Electronic Supplementary Material (ESI) for Materials Horizons.
This journal is © The Royal Society of Chemistry 2023

Supporting Information

4D Printable Liquid Crystal Elastomers with Restricted Nanointerfacial Slippage for Long-Term-Cyclic-Stability Photothermal Actuation

Juzhong Zhang,[a] Shuiren Liu,[a]* Xianghong Wang,[a] Xiaomeng Zhang,[a] Xiaoguang Hu,[a] Linlin Zhang,[a] Qingqing Sun,[a] Xuying Liu[a]*

a. School of Materials Science and Engineering, State Key Laboratory of Structural Analysis, Optimization and CAE Software for Industrial Equipment, Zhengzhou University, Zhengzhou 450001, China.

Corresponding authors: lsrzzdx@zzu.edu.cn(S. Liu); liuxy@zzu.edu.cn(X. Liu).

Materials Preparation

Synthesis of 1D metal nanoparticles(0D-MNP)

The zinc sheets were first cut and flattened, then ultrasonicated in 2.5% sulfuric acid, IPA, and acetone for 30 seconds, 5 minutes, and 5 minutes, respectively, to clean the surface. The sheets were then rinsed with IPA and water and then blown dry with air. The zinc sheets were then immersed in aqueous copper sulfate ($[Cu^{2+}]$ = 12.5 mM) for 30 s. The zinc sheets with thick copper deposits were then immersed in deionized water to quench the reaction, removed, and blown dry. The Zn strips with thick copper deposits were sonicated to obtain copper nanoparticles, and then the particles were washed with water. The particles were then dispersed in acetone and subjected to prolonged sonication to form a dispersion, which was later dried.[1]

Synthesis of functional 1D metal nanoparticles (0D-MNP-DT)

The copper nanoparticles were dispersed into 100 mL of methanol by sonication, and then 50 µL of 1,10-decanedithiol was added. The mixture of copper nanoparticle suspension and thiol was stirred magnetically for 10 min to functionalize on the surface and finally washed with dichloromethane and dried to obtain the functionalized copper nanoparticles.[2]

Synthesis of functional 1D metal nanowires(1D-MNW-OE)

A one-pot oleylamine-assisted solvothermal approach was used to synthesize 1D-MNW, and 100 mg of CuCl was first added to 10.0 mL of oleylamine and dispersed at room temperature. Then it was heated to 130 °C under vacuum for 1 h to remove water and oxygen. Next, 428.13 mg of NaDDTC powder was sonicated in 6.0 ml OM at room temperature to form a dispersion of NaDDTC and was quickly injected into the above solution. The resulting mixture was kept at 260 °C for 15 min. After cooling to room temperature, the mixture was washed several times with ethanol and dried.[3] The obtained material was then treated with oxygen plasma.[4] 100 mg suspension of the obtained material was mixed with 50 mL of ethanol, and 1 mL of 7-octenyltrimethoxysilane was added stepwise and kept at room temperature with constant stirring (500 rpm) for 48 h. For removal of the unreacted 7-octenyltrimethoxysilane molecules, the obtained product was washed with ethanol.

Synthesis of 2D metal nanosheet (2D-MNS)

The materials used in this study were synthesized by selective etching of Al layers from Ti_3AlC_2. One gram of Ti_3AlC_2 powder (< 75 µm particle size) was gradually added to the solution of a mixture of lithium fluoride and hydrochloric acid. The mixture was kept in the water bath for 24 h at 35 °C. After etching, the mixture was washed five times by centrifugation in plastic centrifuge tubes at 3500 rpm for 5 min until the pH of the supernatant reached 6 to obtain multilayer MXene. For delamination, ethanol was used. The powder was then strung with the intercalation reagents, ethanol, for another 20 min under sonication to induce guest intercalation and host layer fragmentation, which was then centrifuged at 10000 rpm to separate the intercalated powder from the intercalation reagents. Last, the obtained precipitate was re-dispersed in water under sonication for 20 min, and then centrifuged at 3500 rpm, and then the supernatant was collected. The supernatant was freeze-dried and collected.

Synthesis of silylation reagents functional 2D metal nanosheets (2D-MNS-AP)

100 mg suspension of $Ti_3C_2T_x$-MXene was mixed with 50 mL of ethanol, and 1 mL of (3-aminopropyl)triethoxysilane (APTES) was added stepwise and kept at room temperature with constant stirring (500 rpm) for 48 h. For removal of the unreacted APTES, the obtained product was washed with a water and ethanol (1:1) mixture.[5]

Synthesis of liquid crystal elastomer composites

Physically blended nanocomposites and the covalently bonded covalent polymer with metal-based nanoparticles were synthesized by a one-pot method. Metal-based nanoparticles were first dispersed in DMF by sonication, forming the monomer and crosslinker dispersion A. Then, 1,4-bis-[4-(6-acryloyloxyhexyloxy)benzoyl-oxy]-2-methylbenzene (RM82), 1,10-decanedithiol (10-DT), tris[2-(3-mercaptopropionyloxy)ethyl] isocyanurate (TEMPIC), and 2,2-dimethoxy-2-phenylacetophenone (DMPA) were dissolved in dispersion A, forming the monomer and crosslinker solution B. dipropylamine was dissolved into DMF solution, forming the catalysis solution C. The solutions B and C were mixed by shaking on a vortex mixer to ensure the formation of a homogeneous dispersion, then poured into a polytetrafluoroethylene mold. Polydomain LCEs were obtained by heating at 60 °C overnight. The samples solvent was removed at 80 °C under vacuum for 24 h. After cooling down to room temperature, the samples were mechanically stretched and placed under a UV light (365 nm) to allow the acrylate-acrylate crosslinking reaction to go to completion and transform it from a polydomain state to a monodomain state. In this system, the ratio of acrylic ester group to mercapto group is roughly 1.1:1, while the sulfhydryl groups of TEMPIC:10-DT in the two thiols have a ratio of 1:9.The addition amount of nano-filler was determined to be 0.2 wt% through preliminary experiments, and Fig. S26 shown the photothermal actuation stress of these materials.

Synthesis of liquid crystal elastomer ink for 4D printing

Metal-based nanoparticles were first dispersed in DCM (six times the weight of the raw materials) by sonication, forming the monomer and crosslinker dispersion A. Then, 1,4-bis-[4-(6-acryloyloxyhexyloxy)benzoyl-oxy]-2-methylbenzene (RM82), 1,10-decanedithiol (10-DT), tris[2-(3-mercaptopropionyloxy)ethyl] isocyanurate, and DMPA were dissolved in dispersion A, forming the monomer and crosslinker solution B. Dipropylamine was dissolved into DCM solution, forming the catalysis solution C. The solutions B and C were mixed by shaking on a vortex mixer to ensure the formation of a homogeneous dispersion. The resulting

mixture was stirred and protected from light at room temperature for 24 h. Then it was heated at 40°C to remove the solvent and obtain LCE ink.

4D printing of liquid crystal elastomers

A bioprinting platform (Regenovo 3D Bio-printer, China) was used to construct the 3d structure. Hopper temperature was set to about 30 °C, the layer highlight was set to 300 μm, the printing speed was 15 mm s^{-1}, and the 365 nm light source power was set to 20%.

Characterization and Measurements

Powder and liquid samples were prepared as discs using potassium bromide (KBr) and FTIR spectra of the samples were collected using an FTIR spectrophotometer(Bruker, TENSOR II), and the FTIR spectra of all LCE samples were collected using the attenuated total reflection (ATR) technique. Dynamic Light Scattering (DLS) measurements and analysis were performed with a Malvern Zetasizer. Differential scanning calorimetry (DSC) analysis was performed under a nitrogen gas atmosphere on a DSC-60 PLUS, and the heating rate was 10 °C min^{-1}. The results discussed in the work were taken from the second heating curves and first cooling curves (the first heating was performed to reduce the thermal history of the tested samples). Optical spectra were acquired with a Cary 5000 UV-VIS-NIR spectrophotometer. To measure the degree of orientation of the LCE samples, two-dimensional wide-angle X-ray diffraction (2D-WAXD) was performed by an X-ray diffractometer (Bruker, D8 Discover) and the sample temperature was controlled by a programmable hot stage THMS600 from Linkam Scientific Instruments. The light source adopts X-ray phototube copper target radiation, and the diffraction angle 2θ scanning range was 5-35°. Herman's orientational order parameter was calculated by Equations (1) and (2):

$$S = \frac{3\left[cos^2\phi\right] - 1}{2} \tag{1}$$

$$\left[cos^2\phi\right] = \frac{\int_0^{\frac{\pi}{2}} I(\phi) sin\phi cos^2\phi d\phi}{\int_0^{\frac{\pi}{2}} I(\phi) sin\phi d\phi} \tag{2}$$

where S is the order parameter, ϕ is the azimuthal angle, and $I(\phi)$ is the azimuthal intensity distribution.

The nanomaterials were visualized by transmission electron microscopy (FEI, Talos F200S). LCE Samples were prepared from the tensile fractured samples surface to analyze the fracture morphology, while the cross-section samples were prepared by cooling (-80 °C) in a cryomicrotome slicer system (Leica, EM UC7 FC7). The LCE samples were visualized by transmission electron microscopy (Thermo Fisher Scientific, Talos L120CG2). Scanning Electron Microscopy (JEOL, JCM-6000Plus) has been used to determine the surface morphology of nanomaterials and LCE samples. Atomic force microscopy (AFM) measurements are performed using a NanoWizard® 4 XP (JPK Instruments, Bruker) to analyze the morphologies of the sample surface and adhesion force. Polarized optical microscopy (POM) images were taken on Leica, DM2700M.

The tensile properties of all LCE samples were carried out with a universal material testing machine (Shimadzu, AGX-S) at a strain rate of 5 mm min^{-1}. For actuating actuation stress testing, NIR actuation of the LCE samples was measured under an 808 nm NIR laser (LASEVER, LSR808H-8W-FC) with the samples were fixed on the universal material testing machine, where the force was controlled at 0.01 N, and a infrared laser (with different power densities) was used to alternately switch and irradiate the samples to explore the relationship between the light power density and actuation stress. An infrared thermal imager (FLIR ONE Pro) was used to measure the relationship between temperature and light power density.

To measure photothermal conversion efficiency (PCE, η) of crosslinkable photothermal metal-based nanomaterials, crosslinkable photothermal metal-based nanomaterials solution (1 ml) were irradiated with 808 nm laser (2 W cm^{-2}) for 10 min to reach the maximum temperature, then the laser was turned off until the temperature down to room temperature via natural cooling. The device was installed in a constant temperature and humidity chamber and the temperature was set to 15 °C to ensure the stability of the ambient temperature. η can be determined from equation (3):

$$\eta = \frac{hS\Delta T_{max}}{I\left(1 - 10^{-A_{808}}\right)} \tag{3}$$

In which, h is the heat transfer coefficient, S represents the container surface area, and ΔT_{max} is the maximum temperature change. I is the laser power (2 W cm^{-2}) and A808 is the absorbance of the samples at wavelength of 808 nm. hS can be calculated from Equation (4):

$$\tau_s = \frac{m_D c_D}{hS} \tag{4}$$

In this equation, m_D is the DMF mass (g) and c_D is the DMF heat capacity (2.059 J g^{-1} K^{-1}). τ_s is the time constant for heat transfer of the system, which can be obtained from the following equation (5):

$$t = -\tau_s \ln(\theta) = -\tau_s \ln\left(\frac{T_t - T_{Surr}}{T_{Max} - T_{Surr}}\right) \tag{5}$$

Where T_t is defined as real-time temperature of crosslinkable photothermal metal-based nanomaterials during the cooling process. T_{Max} stands for the highest temperature, T_{Surr} denotes surroundings temperature. Therefore, the photothermal conversion efficiency η are 57%, 41%, and 79% for 0D-MNP-DT, 1D-MNW-OE, and 2D-MNS-AP materials, respectively.

To determine the material's thermal conductivity λ, we measured the thermal diffusivity (α) using the "laser flash" method with the Netzsch LFA 467. The density (ρ) of the sample was determined by measuring it in ethanol using Archimedes' principle. The specific heat capacities (C_p) were measured by comparing them with a sapphire standard sample. The thermal conductivity λ can be evaluated using the equation (8), and the thermal conductivities of physically blended and covalently bonded 2D-MNS/LCE composites were 0.589 W m^{-1} K^{-1} and 0.605 W m^{-1} K^{-1}, respectively.

$$\lambda = \rho \times C_p \times \alpha \tag{6}$$

Devices preparation

Preparation of flexible smart optical gripper

The Flexible smart optical gripper consists of a bending oriented clamping structure and a helically oriented lifting structure. The clamping structure of the bend is oriented by bending the unoriented LCE bend inward three times to form a square, and the orientation is fixed by secondary crosslinking with UV light. The helical structure is oriented by stretching an unoriented elongated LCE and winding it onto a cylindrical rod, after which it is similarly crosslinked by UV light twice to fix the orientation. After this the two parts of the device are fixed to each other by means of metal wire perforations.

Preparation of crawling robot

The crawling robot consists of a laser-cut acrylic sheet as the main structure, a metal rod as the connecting member, and oriented LCE samples as the power source, and the oriented LCEs are fixed to the metal rods on both sides as described in the main text to provide the power for the movement of the crawling robot.

Preparation of light-powered windmill

The light-powered windmill is composed of a movable outer ring, a movable inner ring, a bracket, a connecting rod, a bearing, and an LCE strip actuator. The main structure (containing the movable outer ring, movable inner ring, and bracket) is prepared by 3D printing using PLA, and the bracket is connected to the movable ring by a connecting rod and fixed to the movable inner ring, utilizing a bearing to reduce its friction. One end of the connecting rod is fixed the other end goes through the bearings connecting the inner ring. Four LCE strip actuators connect the movable inner ring and movable outer ring in four directions.

Preparation of bendable tubular actuators

The bendable tubular actuators are prepared by 4D printing. Using a circular rod fixed to a stepper motor as a substrate for conformal printing, the dense inner layer was first printed using a lower printing speed, then the middle layer was printed using a faster printing speed, and finally the outer layer was printed again using a lower printing speed. In this structure the inner and outer layers are used as supports to enhance structural stability and the middle layer is used as the main power source for the tubular actuator. Considering that the directly printed tubular actuators have lower overall orientation and lower cross-linking, the actuation deformation is smaller and the mechanical properties are poorer. Therefore, the printed tubular actuators were oriented along the length direction and crosslinked with UV light to improve their orientation and enhance their mechanical properties.

Preparation of intelligent solar energy collection system

The intelligent solar energy collection system consists of a bendable tubular a commercially available solar panel, the upper and lower ends of the tubular actuator are connected to customized 3D printed connectors, the lower connector is fixed to the test bench and the solar panel is fixed to the upper connector. A 275 W incandescent light source (~1 W cm^{-2}) was used to mimic solar irradiation, and the open-circuit voltage of the solar panel was recorded in real time using a multimeter (Keithley 6500).

molecular dynamics simulation

In order to study nanoscale load and heat transfer between LCE and a metal-based sheet, the Consistent Valence Force Field (CVFF) was utilized to describe the atomistic interactions. The electrostatic interactions were treated using the particle–particle particle–mesh (PPPM) technique, and an rms accuracy of 10^{-4} was used for the PPPM method. To circumvent potential failure in the simulation arising from an inappropriate initial molecular configuration, the nanocomposite models were initially generated with

optimized structures employing the conjugate gradient method for energy minimization. Subsequently, these models underwent a relaxation period at 300 K in the isothermal-isobaric ensemble (NPT), followed by an additional relaxation at 300 K in the canonical ensemble (NVT). To simulate the heat transfer of the material, 2 ns of simulations were performed to reach the non-equilibrium steady state, and two Langevin thermostats were used as heat source and heat sink. In order to simulate the mechanical behavior of materials, a model of semi-insertion of nanomaterials was established. One end of the polymer structure is fixed to prevent the material from moving, and one end of the nanomaterial is moved to simulate the movement of the nanomaterial in the polymer. All simulations are performed by using the large-scale atomic/ molecular massively parallel simulator (LAMMPS).

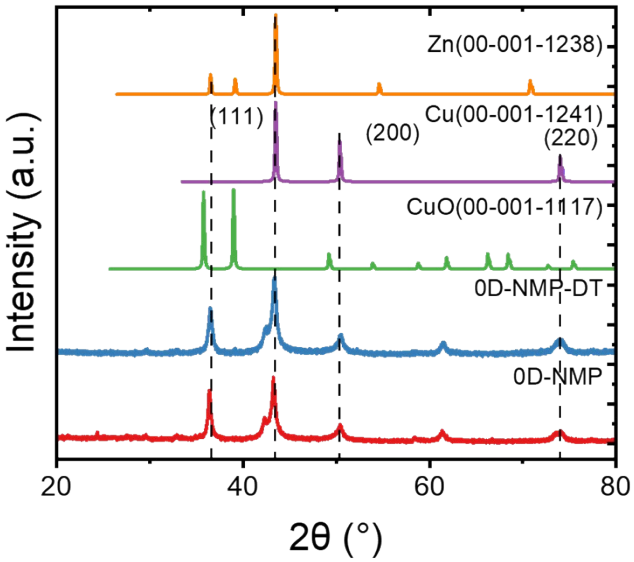

Fig. S1. XRD patterns of 0D-NMP and 0D-NMP-DT in powder form.

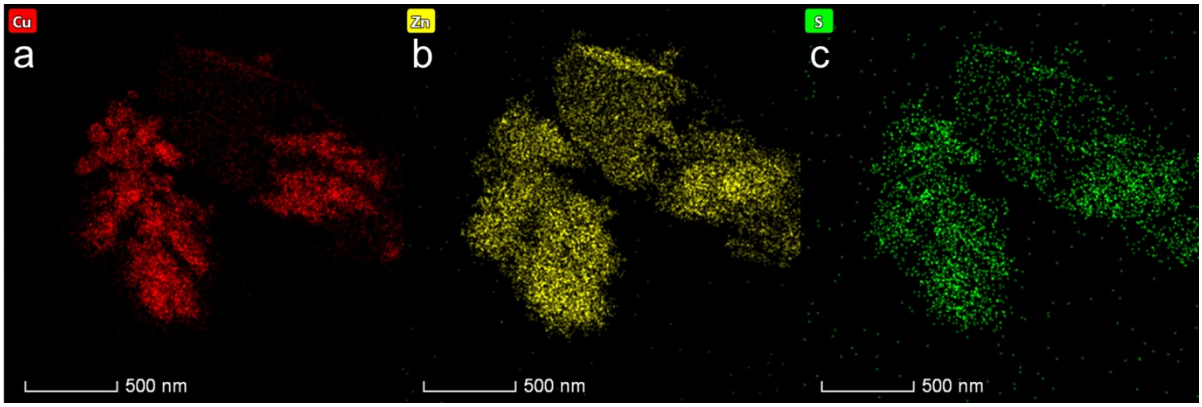

Fig. S2. Elemental analysis by the transmission electron microscopy (TEM)/energy dispersive X-ray spectrometry (EDS) mapping of 0D-MNP-DT (a) TEM/EDS Cu map; (b) TEM/EDS Zn map; (c) TEM/EDS S map. It is clear that some zinc was still attached to the surface of copper nanoparticles during the stripping process of preparing copper nanoparticles, and the presence of sulfur elements proved that thiols were successfully grafted to the surface of the nanoparticles.

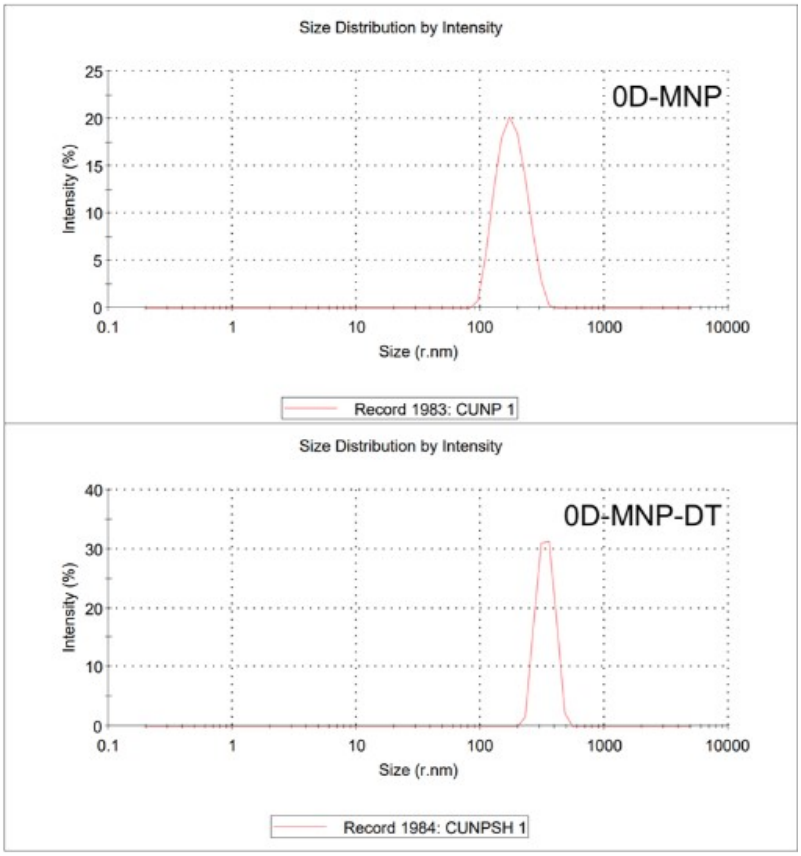

Fig. S3. Particle size distribution curves of copper nanoparticles before and after functionalization.

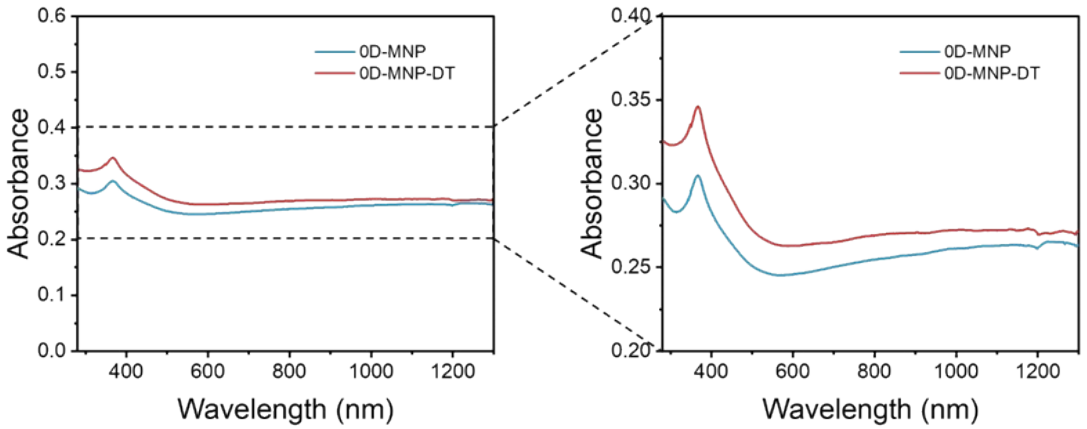

Fig. S4. UV-vis-NIR absorption spectraof copper nanoparticles before and after functionalization.

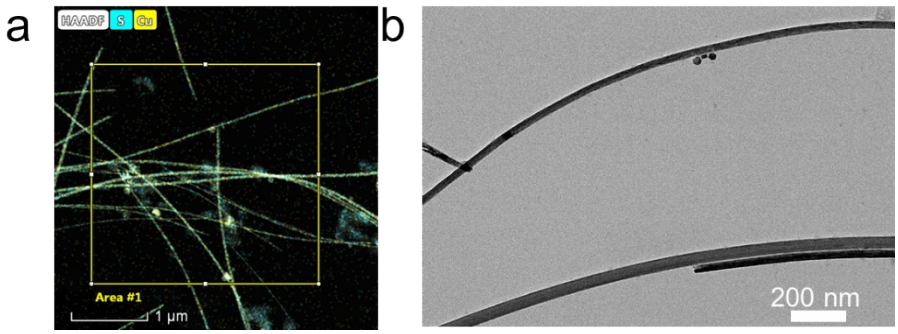

Fig. S5. (a) TEM/EDS elemental mapping images of 1D-MNW. (gray: the high angle annular dark field image, blue: S chemical map, yellow: Cu chemical map) (b) TEM image of 1D-MNW. It can be seen that the prepared uniform nanowires are tens of nanometers in diameter.

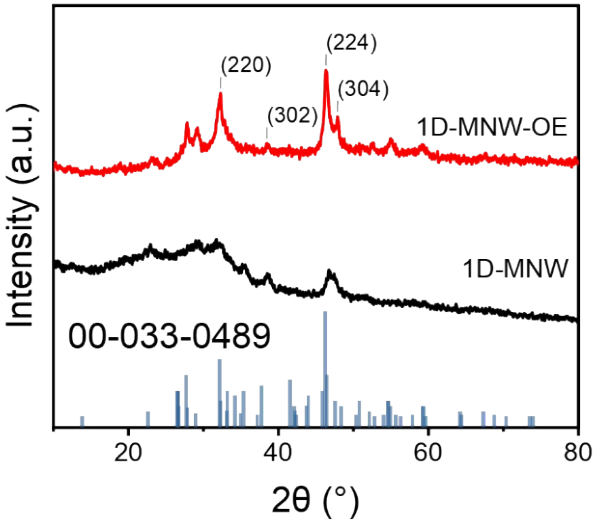

Fig. S6. X-ray diffraction (XRD) patterns for 1D-MNW and 1D-MNW-OE in powder form. The XRD pattern of CuSNW is also similar to Cu_7S_4 (JCPDS 033-0489), a series of diffraction peaks at 31.8°,38.5°, 46.7°, and 47.4° are well indexed to the (220), (302), (224) and (304) facets of Cu_7S_4.

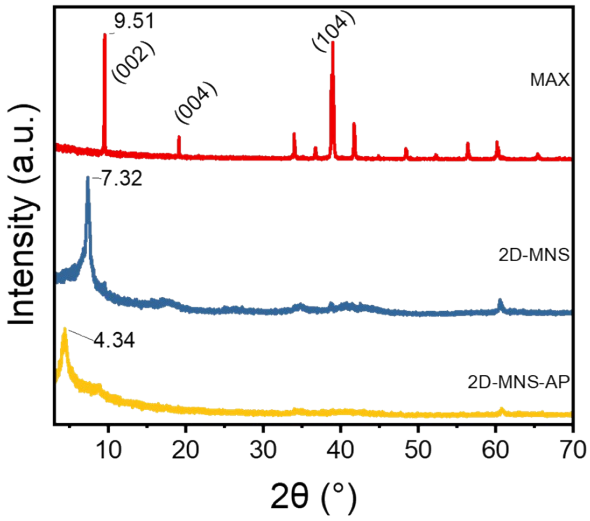

Fig. S7. XRD patterns for 2D-MNS in powder form. The interlayer spacing of the nanosheets was calculated according to the Bragg diffraction equation with the peak from the (002) crystal plane of MXene, and it shows that the interlayer spacing d changed from 1.21 to 2.03 nm after functionalization.

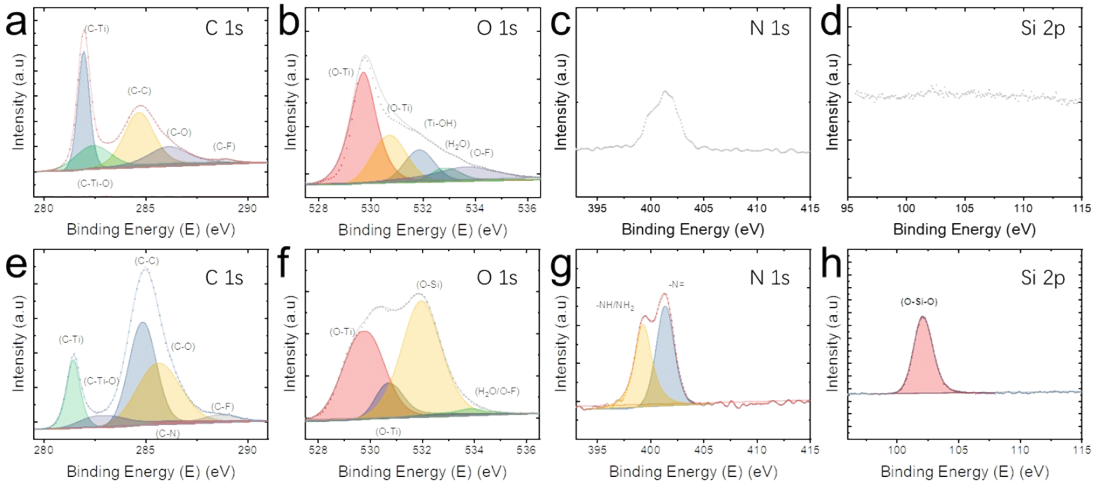

Fig. S8. X-ray photoelectron spectroscopy (XPS) was used to confirm the functionalization of 2D-MNS. XPS spectra of the raw 2D-MNS nanosheet: (a) XPS-O1s, (b) XPS-O1s, (c) XPS-N1s and (d) XPS-Si2p spectra.; XPS spectra of the 2D-MNS-AP nanosheet: (e) XPS-O1s, (f) XPS-O1s, (g) XPS-N1s and (h) XPS-Si2p spectra. In the O 1S region, the fitted peak of O-OH is replaced by a large intensity peak of O-Si after APTES functionalization. In the N 1S and Si 2p region, the presence of -NH/NH_2, -N=, and O-Si-O peaks in 2D-MNS-AP confirm APTES functionalization.

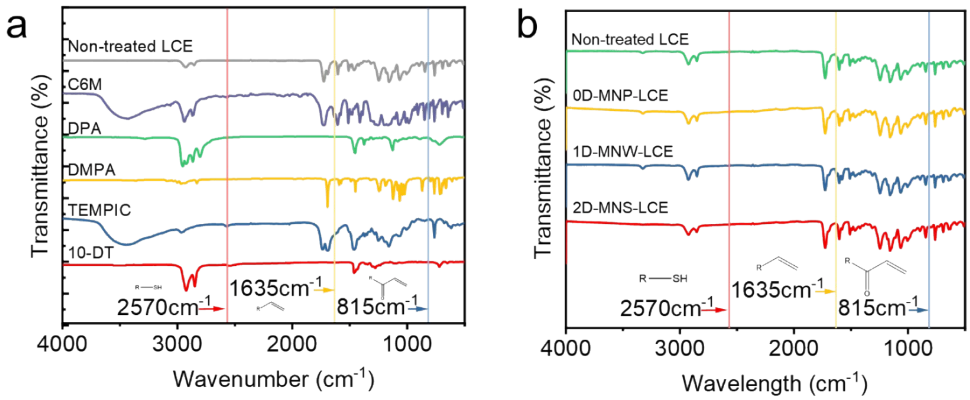

Fig. S9. (a) Fourier transform infrared (FTIR) spectra of LCE and raw materials. (b) FTIR spectra of different LCE samples. The disappearance of both thiols and acrylates as indicated by the vibration of -SH (2570cm^{-1}) and double bond (815cm^{-1}) peaks in all samples demonstrated the successful synthesis of the LCE.

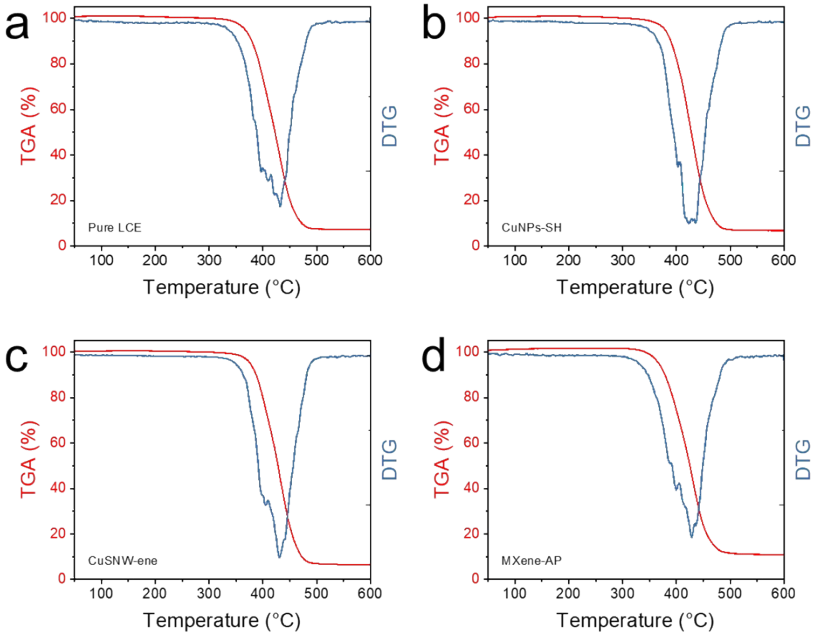

Fig. S10. The decomposition temperatures were analyzed by means of thermogravimetric analyses (TGA). Thermogravimetric and thermogravimetric derivative curves for (a) non-treated LCE sample, (b) 0D-MNP-LCE sample, (c) 1D-MNW-LCE sample, and (d) 2D-MNS-LCE sample at a heating rate of 10°C/min. The addition of nanofillers had a minor effect on the stability of the LCE samples, and all the samples have no samples decomposition were occurring below 300℃.

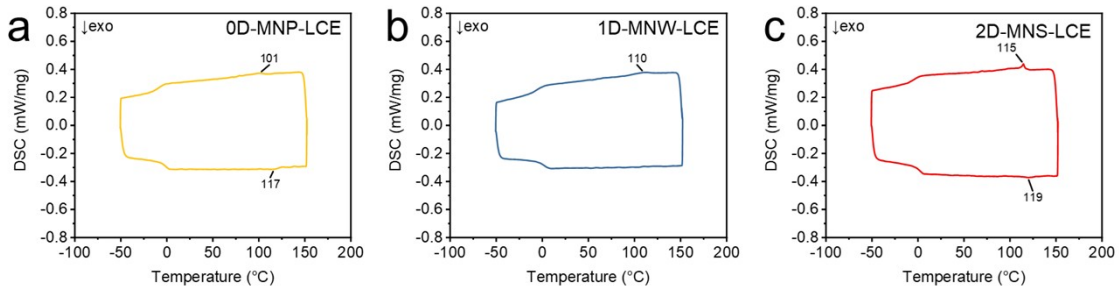

Fig. S11. Differential scanning calorimetry (DSC) was used to identify the nematic to isotropic transition temperature, TNI of the LCE samples. (a) 0D-MNP-LCE sample, (b) 1D-MNW-LCE sample, (c)2D-MNS-LCE sample during the first cooling and second heating cycles. The endothermic peak can be observed at a temperature of approximately 101°C,110°C, and 115°C indicating a transition between the nematic and isotropic states present in the LCE. Compared with pure LCE, covalently bonded samples had higher phase transition temperature.

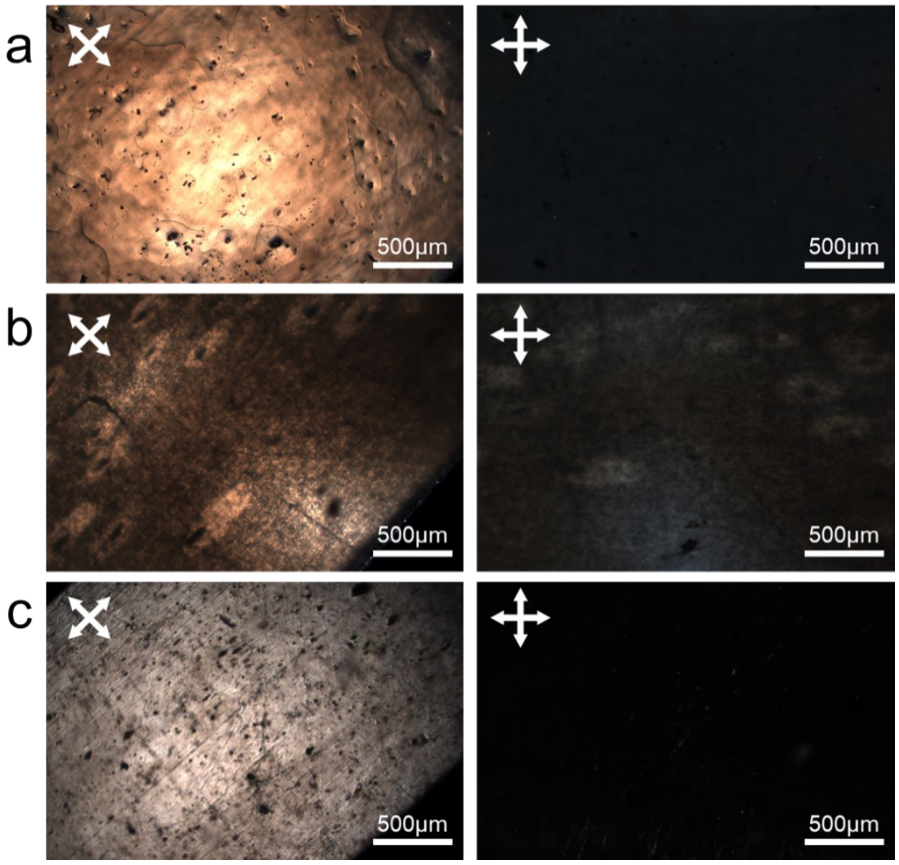

Fig. S12. Orientation analysis of the LCE samples were studied by Polarized optical micrographs (POM). POM images of the (a) Non-treated LCE sample, (b) 0D-MNP-LCE sample, and (c) 1D-MNW-LCE sample under crossed polarizers that were rotated 45° from each other. The brightness is minimized when the uniaxial tension axis is parallel to the analyzer (right) and maximized when the uniaxial tension axis is rotated at 45° to either the polarizer or analyzer (left), which means that all the LCE samples are well oriented.

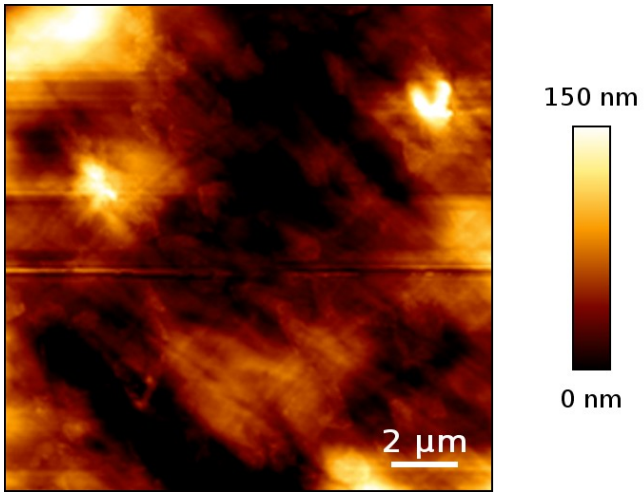

Fig. S13. Atomic force microscopy (AFM) hight mapping image of 2D-MNS-LCE. Since the samples were prepared by using cryo-ultramicrotomy, the surface of the samples was relatively flat, and the slight surface undulations may be due to uneven stresses during processing.

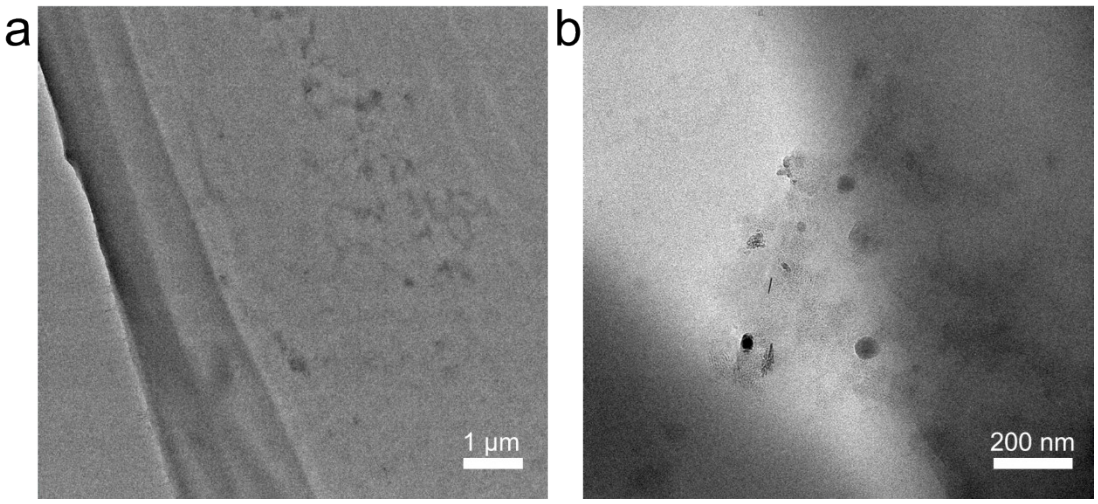

Fig. S14. TEM image of 2D-MNS-LCE. MXene nanosheets are individually and randomly dispersed in the LCE matrix without detectable aggregation. This suggests that functionalization MXene nanosheets have a good compatibility with LCE matrix.

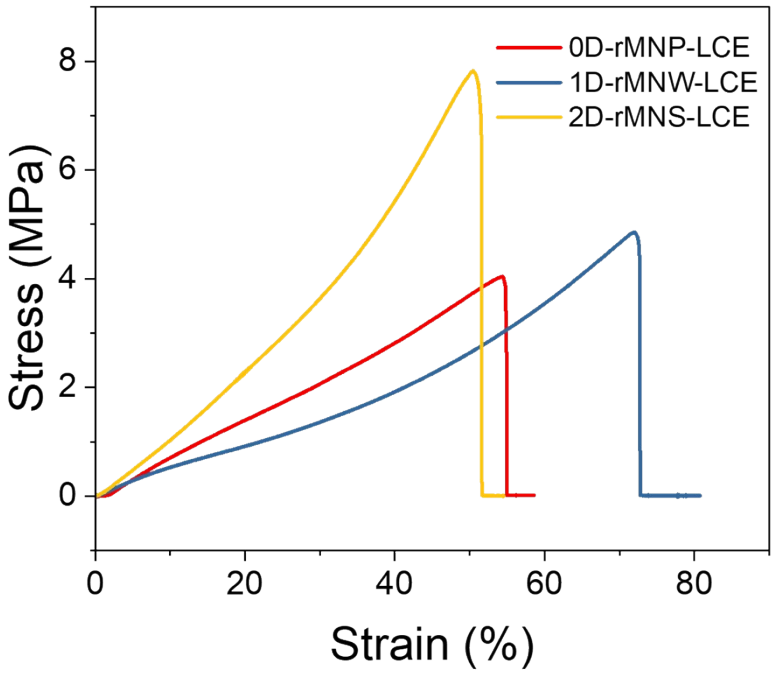

Fig. S15. Stress-strain curves of Physically blended LCE samples.

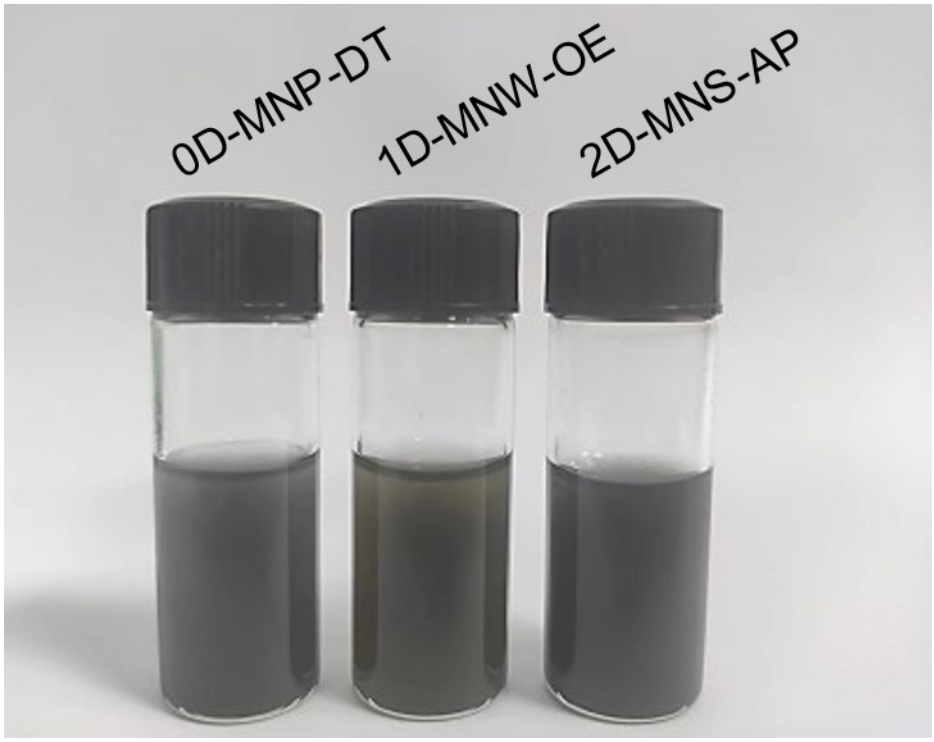

Fig. S16. Optical photograph of the dispersed functionalized nanomaterials in solvent.

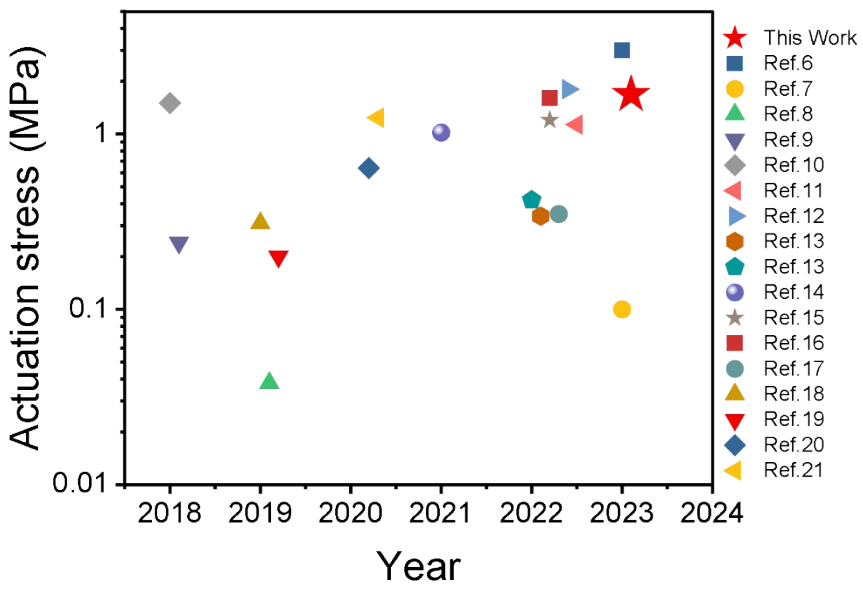

Fig. S17. Comparison of actuation stress of different liquid crystalline elastomers.[6–21]

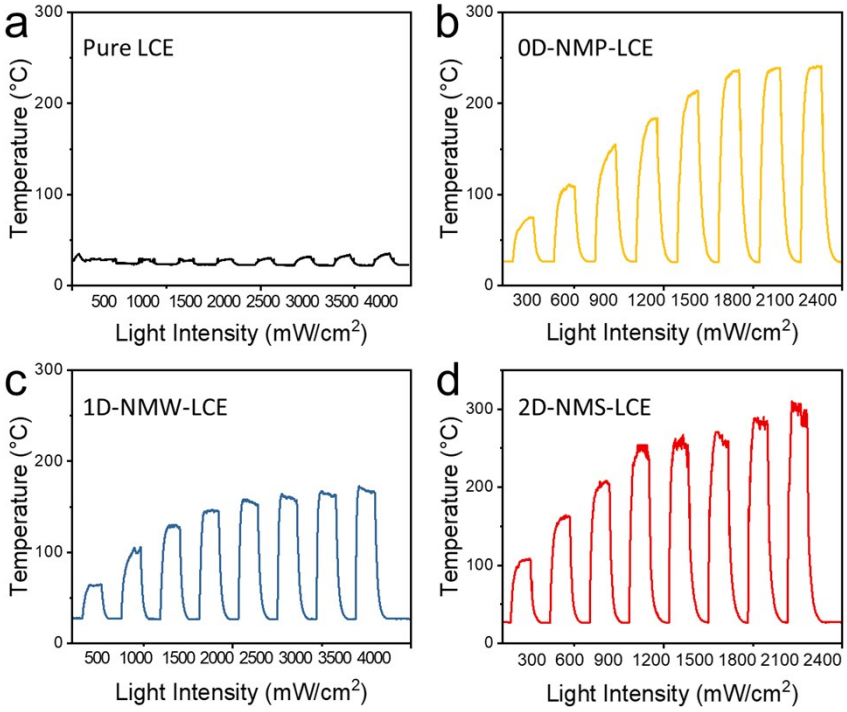

Fig. S18. Power dependence of (a) pure LCE sample, (b) 0D-MNP-LCE sample, (c) 1D-MNW-LCE sample, (d) 2D-MNS-LCE sample for 808 nm NIR light. The light/dark cycle was adjusted to 120 s lights-on and 120 s lights-off. The maximum temperature of the material surface increasing with the laser power.

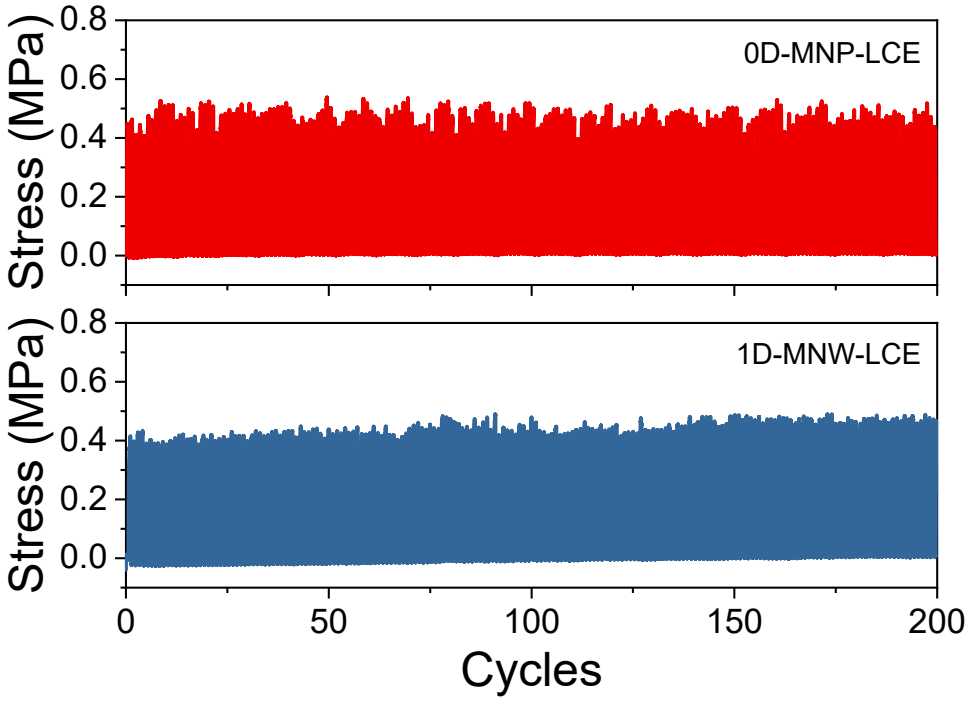

Fig. S19. Stability of the covalently bonded 0D-MNP-LCE and 1D-MNW-LCE under 808 nm light.

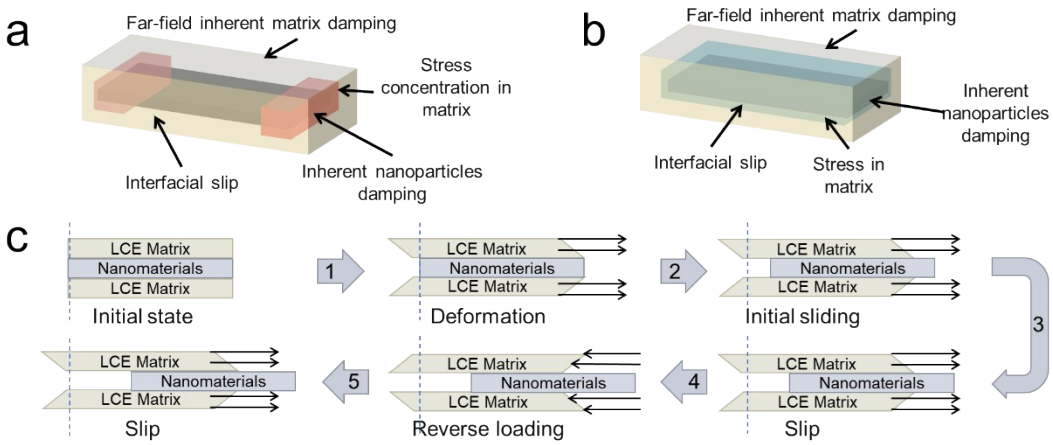

Fig. S20. (a) Schematic representation of internal interactions during deformation of physically blended composites. (b) Schematic representation of internal interactions during deformation of the covalently bonded composite. (c) Schematic representation of nanomaterials slippage during loading.

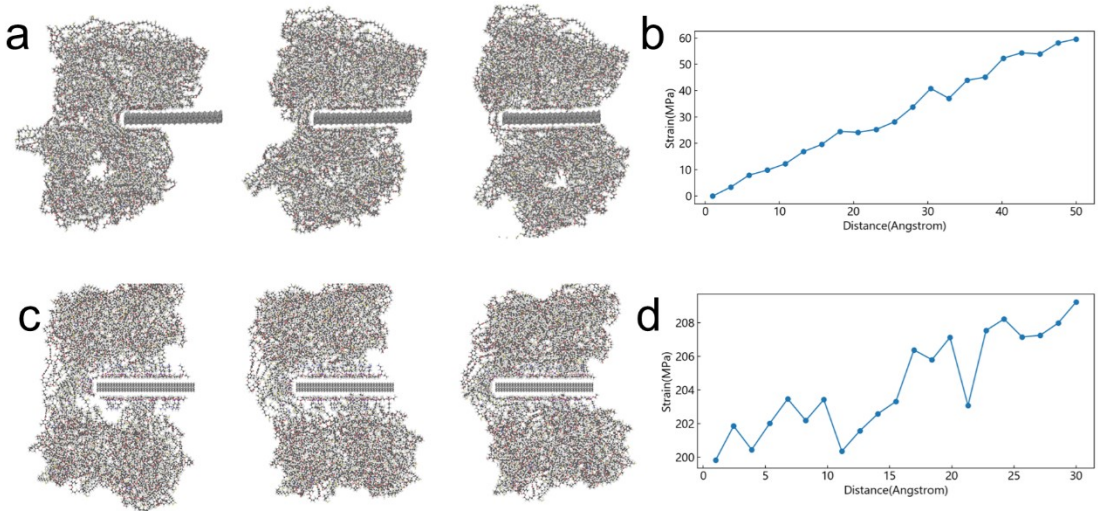

Fig. S21. (a) The snapshots of the atomic configuration of nanocomposite. (b) The strain-displacement curve during push-in of physically blended LCE. (c) The snapshots of the atomic configuration of nanocomposite and (d) the strain-displacement curve during push-in of covalently bonded LCE. To highlight the differences in covalent bonding we will simplify the 2D-MNS with APTES attached into a whole structure.

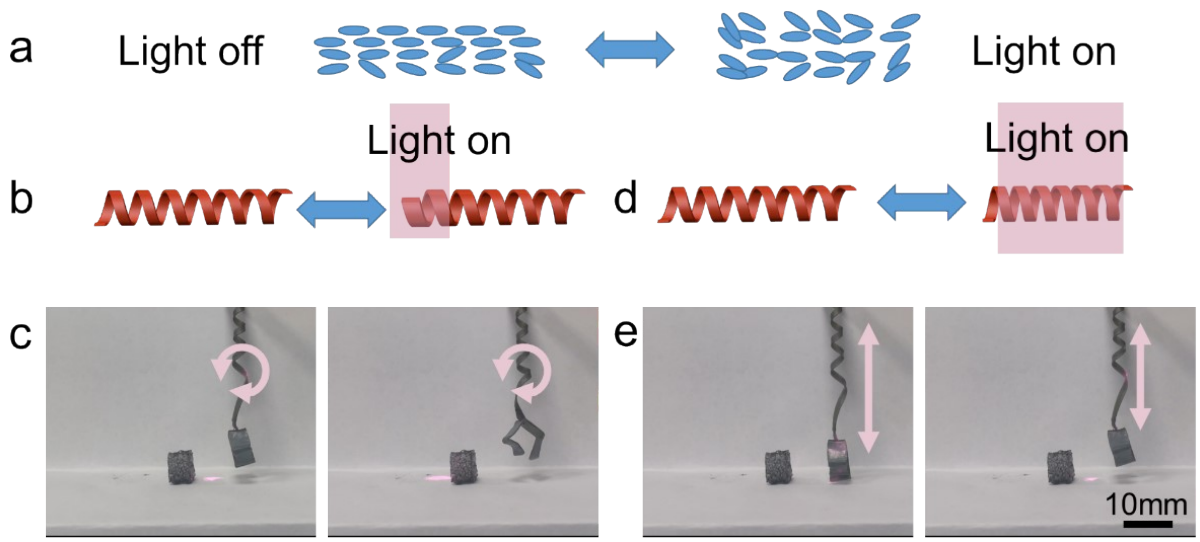

Fig. S22. Motion modes of lifting structure. (a) Arrangement of mesogens in the spring-shaped LCE actuator and their changes when it's exposed to light. (b) When the size of the light spot projected onto the sample is smaller than the pitch of a single helix, the previously bent LCEs tend to transform into a flat structure, (c) causing the actuator to rotate; (d) When the size of the light spot projected onto the sample is much larger than the helix, (e) the actuator undergoes contraction first.

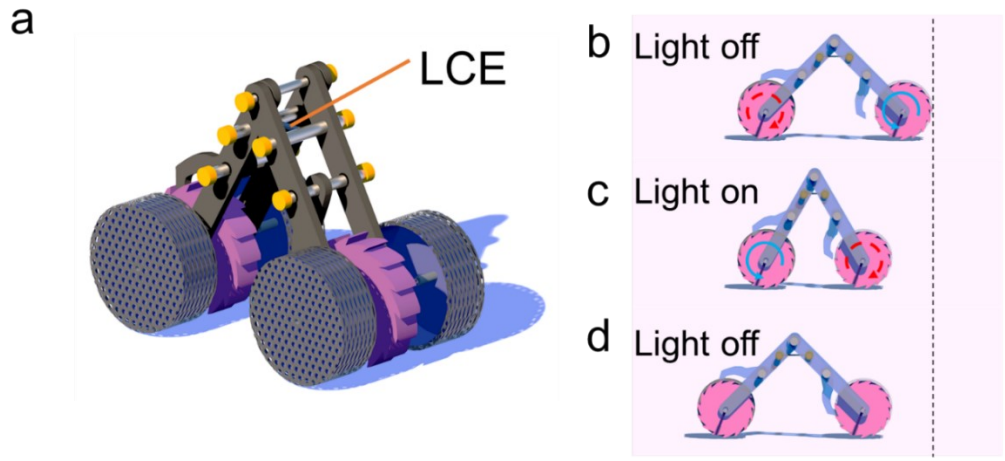

Fig. S23. (a) Schematic diagram of the LCE unidirectional crawling robot (b-d) Schematic diagram of the mechanism of unidirectional motion of the crawling robot. Once exposed to light, the shrink of the LCE actuator leads to a smaller angle between the beams and frames, so that the spacing between the two wheels is reduced. In addition, the ratcheting structure of the front wheel prevents its clockwise rotation, and the ratcheting wheel of the rear wheel does not directly contact the rear wheel, so that the rear wheel can move forward normally. When the light source is turned off, the temperature of the LCE decreases and its length increases. The existence of gravity causes a tendency for the two wheels to move outward, but the presence of the ratchet wheel on the rear wheel prevents it from moving backward. By repeating these two steps, the crawling robot will move forward intermittently when exposed to intermittent light.

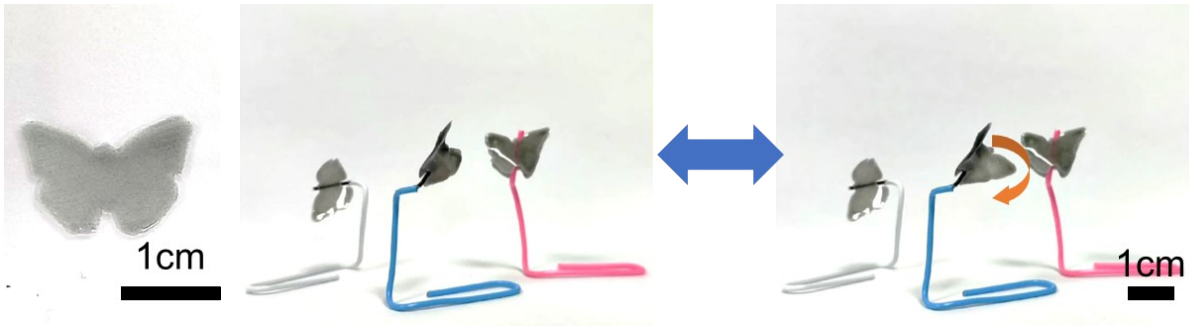

Fig. S24. Optical images of the butterfly-shaped covalently bonded LCE samples and flapping their wings in the light.

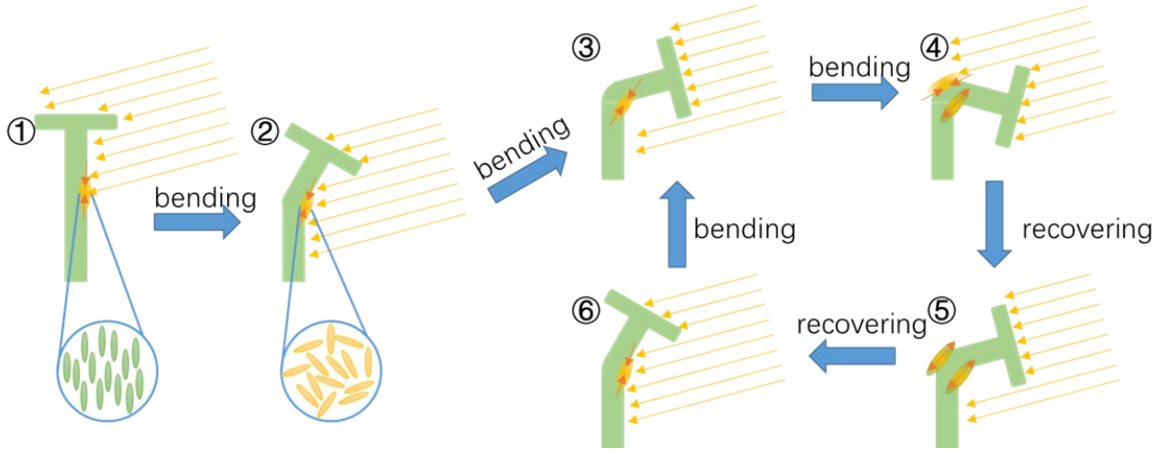

Fig. S25. Mechanism of the phototropic movement of the smart solar energy collection system.

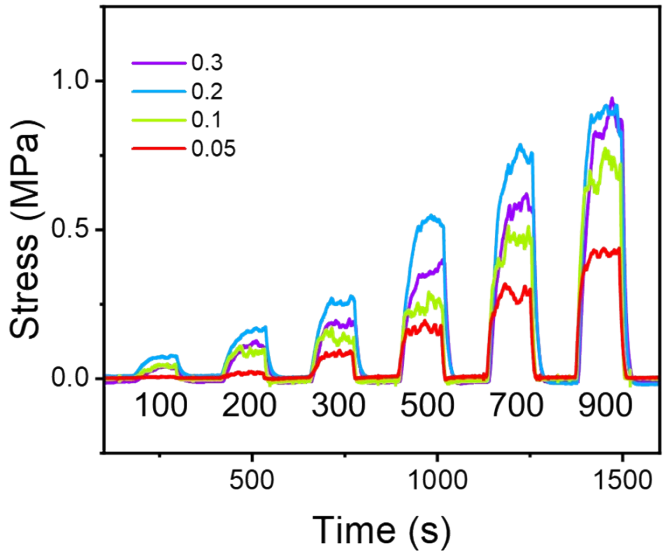

Fig. S26. Photothermal performance of liquid crystalline elastomers with different 2D-MNS-AP contents (wt%). (The value below the curves is the power of 808 nm near-infrared light source, the units are in mW/cm^2)

Table S1 Young's modulus, Maximal stress, and Elongation at break data of different liquid crystal elastomers with different metal nanomaterials.

Sample name	Young's modulus (MPa)	Maximal stress (MPa)	Elongation at break (%)
Pure LCE	5.82±2.13	4.30±0.47	43.99±5.84
0D-rMNP-LCE	9.55±3.79	5.31±1.03	57.50±13.28
1D-rMNW-LCE	5.19±0.62	3.43±0.95	67.47±10.80
2D-rMNS-LCE	8.81±1.48	7.53±0.63	53.54±2.13
0D-MNP-LCE	7.56±2.16	4.14±0.34	53.67±5.89
1D-MNW-LCE	13.83±4.02	6.28±1.75	51.52±0.97
2D-MNS-LCE	8.16±1.58	6.32±0.33	63.43±6.17

Movie S1. Flexible smart optical gripper controlled by an 808 laser light to grab and move the object.

Movie S2. A crawling robot can move in one direction by controlling the light switch.

Movie S3. The windmill rotates spontaneously when the light is on.

Movie S4. Butterfly-shaped 3D printed LCE samples flapping their wings in the light.

References

1 Y. Lin, Z. Chen, L. Fang, M. Meng, Z. Liu, Y. Di, W. Cai, S. Huang and Z. Gan, *Nanotechnology*, 2018, **30**, 015402.
2 G. A. Gelves, B. Lin, U. Sundararaj and J. A. Haber, *Nanotechnology*, 2008, **19**, 215712.
3 N. Li, D. Yin, L. Xu, H. Zhao, Z. Liu and Y. Du, *Mater. Chem. Front.*, 2019, **3**, 394–398.
4 Y. Rodríguez-Lazcano, H. Martínez, M. Calixto-Rodríguez and A. Núñez Rodríguez, *Thin Solid Films*, 2009, **517**, 5951–5955.
5 S. Kumar, Y. Lei, N. H. Alshareef, M. A. Quevedo-Lopez and K. N. Salama, *Biosens. Bioelectron.*, 2018, **121**, 243–249.
6 Y. Wang, Q. He, Z. Wang, S. Zhang, C. Li, Z. Wang, Y. Park and S. Cai, *Adv. Mater.*, 2023, **35**, 2211283.
7 R. Annapooranan, Y. Wang and S. Cai, *Adv. Mater. Technol.*, 2023, **8**, 2201969.
8 D. J. Roach, C. Yuan, X. Kuang, V. C.-F. Li, P. Blake, M. L. Romero, I. Hammel, K. Yu and H. J. Qi, *ACS Appl. Mater. Interfaces*, 2019, **11**, 19514–19521.
9 Z. Wang, K. Li, Q. He and S. Cai, *Adv. Mater.*, 2019, **31**, 1806849.
10 H. Tian, Z. Wang, Y. Chen, J. Shao, T. Gao and S. Cai, *ACS Appl. Mater. Interfaces*, 2018, **10**, 8307–8316.
11 H.-F. Lu, Z.-Z. Nie, H. K. Bisoyi, M. Wang, S. Huang, X.-M. Chen, Z.-Y. Liu and H. Yang, *Sci. China Mater.*, 2022, **65**, 1679–1686.
12 T. Zhao, Y. Zhang, Y. Fan, J. Wang, H. Jiang and J. Lv, *J. Mater. Chem. C*, 2022, **10**, 3796–3803.
13 S. Choi, B. Kim, S. Park, J.-H. Seo and S. Ahn, *ACS Appl. Mater. Interfaces*, 2022, **14**, 32486–32496.
14 J. Liu, Y. Gao, H. Wang, R. Poling-Skutvik, C. O. Osuji and S. Yang, *Adv. Intell. Syst.*, 2020, **2**, 1900163.
15 J. Gong, P. Cao, J. Yang, Z. Tang, X. Zhang, Q. Wang, T. Wang, X. Pei and Y. Zhang, *Macromol. Mater. Eng.*, 2022, **307**, 2200354.
16 T. Zhao, W. Fang, Y. Fan, Z. Hu, H. Wu, X. Feng and J. Lv, *Adv. Mater. Technol.*, 2022, **7**, 2101660.
17 Q. He, Z. Wang, Y. Wang, A. Minori, M. T. Tolley and S. Cai, *Sci. Adv.*, 2019, **5**, eaax5746.
18 C. Zhang, X. Lu, G. Fei, Z. Wang, H. Xia and Y. Zhao, *ACS Appl. Mater. Interfaces*, 2019, **11**, 44774–44782.
19 Y. Wang, Z. Wang, Q. He, P. Iyer and S. Cai, *Adv. Intell. Syst.*, 2020, **2**, 1900177.
20 A. F. Minori, Q. He, P. E. Glick, I. Adibnazari, A. Stopol, S. Cai and M. T. Tolley, *Smart Mater. Struct.*, 2020, **29**, 105003.
21 Z.-C. Liu, B. Zuo, H.-F. Lu, M. Wang, S. Huang, X.-M. Chen, B.-P. Lin and H. Yang, *Polym. Chem.*, 2020, **11**, 3747–3755.